PNAS RESEARCH ARTICLE | ENGINEERING

Analytical solutions for light propagation of LED

Haohui Zhang[a,1], Kaiqing Zhang[a,b,1], Mingzheng Wu[c,1], Shupeng Li[a], Kevin L. Bodkin[d], Yevgenia Kozorovitskiy[d], John A. Rogers[c,e,f,g,h,2], and Yonggang Huang[a,c,e,g,2]

Affiliations are included on p. 8.

Contributed by Yonggang Huang; received April 6, 2025; accepted July 14, 2025; reviewed by Xue Feng, Jerry Qi, and Sihong Wang

Analytical solutions of diffusion theory for light propagation in turbid media are essential for optical diagnostics and therapeutic applications, including cerebral oximetry, hemodynamic monitoring, and photostimulation. While existing solutions work reasonably well for collimated light sources—lasers and optical fibers—analytical solutions for LEDs remain missing, despite the growing use of LEDs in wearable and implantable bioelectronics. We present a method to solve the diffusion theory and derive analytical solutions for two biomedically relevant configurations: 1) surface-mounted LEDs on semi-infinite media (e.g., wearable devices) and 2) embedded LEDs in infinite media (e.g., implantable devices). Beyond a distance of 4 times the scattering length of the medium to the LED source, our analytical solutions are reasonably accurate, within 6% error for 1) and 3% for 2). This represents significant improvements over existing analytical solutions, characterized by 26% and 15% error, respectively. Using our analytical solutions, we derive tissue optical properties (μ_a and μ_s') from diffuse reflectance results with <7% error, and we determine the irradiance threshold for photostimulation, aligned with experimental optogenetic activation data. Our analytical solutions are readily adaptable to various biomedical applications, offering a rigorous theoretical foundation for next-generation LED-based bioelectronics, to enable more accurate optical diagnostics and therapies in clinical applications.

diffusion theory for light propagation | analytical solution | irradiance threshold | tissue optics | LED

Significance

LEDs are widely used in optical diagnostics and therapy, yet analytical solutions for their light propagation remain lacking. We derive analytical solutions of light propagation for surface-mounted LEDs and embedded LEDs in medium, providing accurate light intensity profiles and diffuse reflectance results. These solutions enable precise derivation of tissue optical properties and determination of irradiance threshold for photostimulation. This work establishes a rigorous theoretical foundation for LED-based bioelectronics, enhancing the accuracy of optical diagnostics and therapies in biomedical applications.

Modeling of light propagation in turbid media, particularly biological tissues, is crucial for noninvasive assessment of physiological states such as tissue oxygenation, hemodynamics, and metabolic activity (1–11). Conventional light propagation models have predominantly focused on collimated light sources like lasers or optical fibers, with light transport modeled using Monte Carlo (MC) simulations (12, 13) or diffusion theory (14–18). These light sources, however, face challenges in miniaturization, wireless connection, and reducing energy consumption when applied to emerging wearable bioelectronics, where light-emitting diodes (LEDs) are increasingly adopted due to their compact size, wireless capability, and energy efficiency (19–23).

MC simulations offer high accuracy for both collimated and diffuse light sources (e.g., LED) by tracking individual photon paths, but their computational cost becomes prohibitive, especially for predicting intensity distributions at large source-detector separations (12, 13, 24, 25). In contrast, diffusion theory provides a computationally efficient approximation that becomes accurate at distances from the source that are much larger than the scattering length of the medium. The existing solution to diffusion theory depends on an accurate source description (16, 18, 26–28) and is given in *SI Appendix*, Eqs. **S3** and **S4**. For the collimated source, the incident light is typically approximated as an isotropic point source located at a depth of $1/(\mu_a + \mu_s')$ within the medium (29–32), where μ_a and μ_s' denote the absorption and reduced scattering coefficients of the medium, respectively. Accordingly, the incident energy at the boundary drops to zero, thereby defining the boundary condition. For a point collimated source (Fig. 1*A*) on the boundary of a semi-infinite medium ($\mu_a = 0.005\ \text{mm}^{-1}$ and $\mu_s' = 2\ \text{mm}^{-1}$), MC simulations are compared with the existing analytical solution of the diffusion theory (Fig. 1 B and 1C). They agree very well (~6% error) for distance to the source beyond 11 times of the scattering length $1/\mu_s'$ of the medium (*SI Appendix*, Fig. S1*B*).

In contrast to light from a collimated source irradiating in a single direction (Fig. 1*A*), light from an LED exhibits incident directions distributed across a hemisphere (Fig. 1*D*), with an angular distribution typically described by the Lambertian emission profile (26, 33–35). Consequently, the intensity distribution within the medium for an LED source (Fig. 1*E*) differs significantly from that for a collimated source (Fig. 1*B*) for identical

Author contributions: H.Z., K.Z., J.A.R., and Y.H. designed research; H.Z., K.Z., M.W., and Y.H. performed research; H.Z., M.W., S.L., K.L.B., and Y.K. analyzed data; and H.Z., K.Z., M.W., Y.K., J.A.R., and Y.H. wrote the paper.

Reviewers: X.F., Tsinghua University; J.Q., Georgia Institute of Technology; and S.W., University of Chicago.

Competing interest statement: Prof. Sihong Wang, and one of the authors, Prof. John A. Rogers, have previously co-authored a review article together that included more than 130 authors. Apart from this, they have no other competing interests.

[1]H.Z., K.Z., and M.W. contributed equally to this work.

[2]To whom correspondence may be addressed. Email: jrogers@northwestern.edu or y-huang@northwestern.edu.

This article contains supporting information online at https://www.pnas.org/lookup/suppl/doi:10.1073/pnas.2508163122/-/DCSupplemental.

Published August 13, 2025.

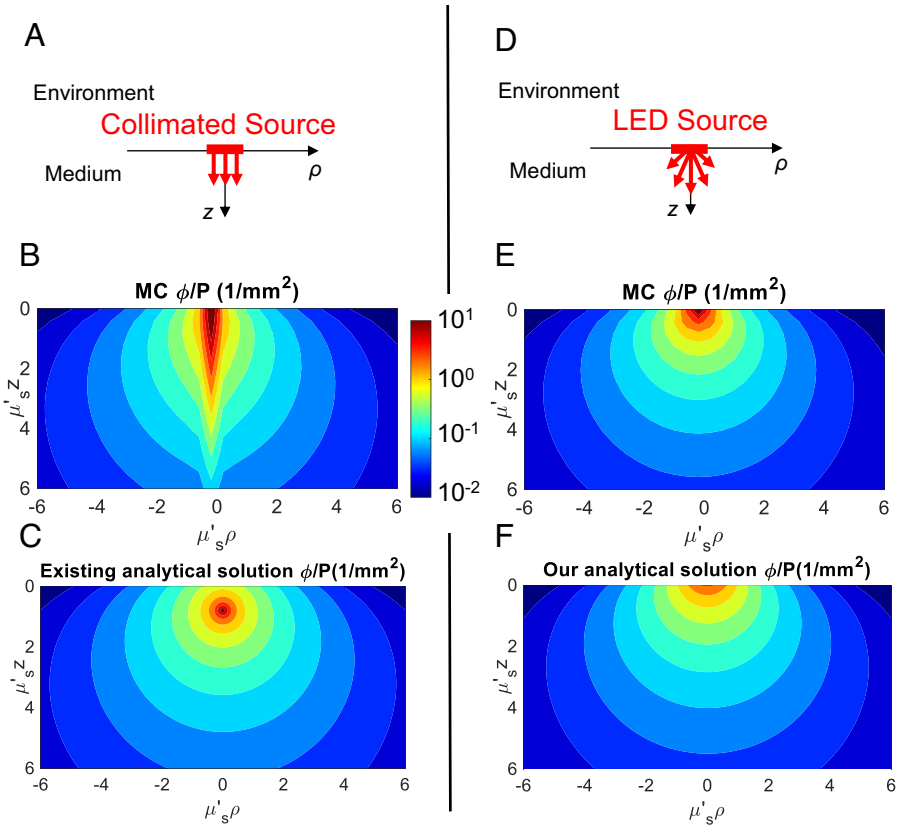

Fig. 1. Comparison between collimated and LED light sources. (*A*) Schematic of a collimated source on a semi-infinite medium. (*B*) Intensity profile ϕ, normalized by power P for a point collimated source, obtained by MC simulation. (*C*) Normalized intensity profile (ϕ/P) from the existing analytical solution to the diffusion theory. (*D*) Schematic of an LED source on a semi-infinite medium. (*E*) Intensity profile ϕ, normalized by power P for a point LED source, obtained by MC simulation. (*F*) Normalized intensity profile (ϕ/P) from our analytical solution to the diffusion theory.

total incident power and material properties. The intensity distribution for an LED source does not agree well with the existing analytical solution of the diffusion theory (Fig. 1*C*) either. Fig. 1*F* shows our analytical solution of diffusion theory for an LED source, to be shown in this paper, and it agrees very well (~6% error) with MC simulations for the same LED source (Fig. 1*E*) in the entire medium except within 4 times the scattering length $1/\mu_s'$ of the medium to the source.

In this paper, we propose a method to obtain the analytical solution of the diffusion theory for an LED source on a semi-infinite medium. This accurate solution enables reliable derivation of absorption coefficient (μ_a) and reduced scattering coefficient (μ_s') from LED-based diffuse reflectance measurements, which is critical for brain oxygen monitoring, cerebral hemodynamic assessment, and photobiomodulation (36–41). Furthermore, for an LED source embedded in an infinite medium, we also obtain an analytical solution of the diffusion theory, and apply it to estimate the irradiance threshold required for opsin activation during in vivo optogenetic stimulation in the mouse brain (42), demonstrating its practical utility in biomedical applications and neuroscience research.

Results and Discussion

Diffusion Theory for Light Propagation. Light propagation in media exhibiting both absorption and scattering is governed by the radiative transfer equation (32, 43, 44), which can only be solved by numerical methods such as MC simulation. For highly scattering media such as biological tissues, the radiative transfer equation is simplified to the following diffusion equation (16, 32, 45):

$$\mu_a\phi - D\nabla^2\phi = S(\mathbf{r}), \quad [1]$$

where $D = \frac{1}{3(\mu_a+\mu_s')}$ is the diffusion coefficient, μ_a and μ_s' are the absorption coefficient and reduced scattering coefficient, respectively, $S(\mathbf{r})$ is the power of the light source at position $\mathbf{r}$ and is assumed to be isotropic in the diffusion theory, the intensity $\phi(\mathbf{r})$ denotes the energy flow rate per unit projected area at position $\mathbf{r}$. The current density $\mathbf{J}(\mathbf{r}) = -D\nabla\phi$ is the net energy flow rate per unit area.

For a boundary with unit normal vector $\mathbf{n}$ (Fig. 2*A*), the total intensities leaving and entering the medium at the boundary are (32, 45)

$$I_{out} = \frac{1}{4}\phi + \frac{1}{2}\mathbf{J}\cdot\mathbf{n}, \quad [2]$$

$$I_{in} = \frac{1}{4}\phi - \frac{1}{2}\mathbf{J}\cdot\mathbf{n}. \quad [3]$$

Physically, I_{out} represents the intensity of photons scattered within the medium and propagating outward across the boundary. In contrast, I_{in} denotes the intensity of photons entering the medium, which results from partial reflection of I_{out} and from a boundary source emitting light into the medium.

For a scattering medium immersed in an environment with the same refractive index n, such as (approximately) biological tissues in water (46–48), no light is reflected back into the medium at the boundary. In addition, in the existing theory for the collimated source, the incident light is typically approximated as an isotropic point source located at a depth of $1/(\mu_a+\mu_s')$ within the medium (29–32) (*SI Appendix*, Fig. S1*A*). As a result,

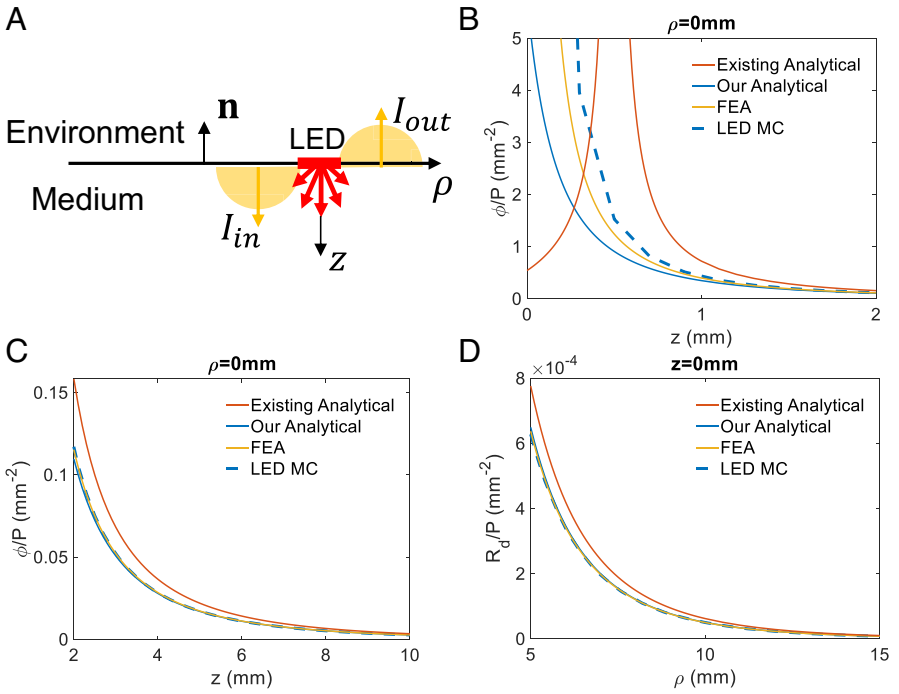

Fig. 2. Validation of our analytical solution against MC simulations. (*A*) Schematic of an LED source on the boundary of a semi-infinite medium, showing light propagation outward in the *Top* hemisphere I_{out} and inward in the *Bottom* hemisphere I_{in}. Comparison of normalized intensity and diffuse reflectance computed using Monte Carlo (MC) simulations, finite element analysis (FEA), and analytical solutions. Normalized intensity ϕ/P versus depth z at ρ = 0 mm. (*B*) Near field. (*C*) Far field. (*D*) Normalized diffuse reflectance R_d/P.

$$I_{in} = \frac{1}{4}\phi - \frac{1}{2}\mathbf{J}\cdot\mathbf{n} = 0, \quad [4]$$

at the boundary, and this is called the refractive-index-matched boundary condition (32). For the refractive-index-mismatched boundary resulting from a scattering medium immersed in an environment with different refractive indices (e.g., biological tissues in air), I_{in} equals the portion of I_{out} that is reflected back into the medium (26, 45)

$$I_{in} = \frac{1}{4}\phi - \frac{1}{2}\mathbf{J}\cdot\mathbf{n} = \frac{R_\phi}{4}\phi + \frac{R_J}{2}\mathbf{J}\cdot\mathbf{n}, \quad [5]$$

at the boundary, where the effective reflectances $R_\phi = \int_0^{\frac{\pi}{2}} 2\ \sin\ \theta\ \cos\ \theta\ R_F(\theta, n)\ \mathrm{d}\theta$ and $R_J = \int_0^{\frac{\pi}{2}} 3\ \sin\ \theta\ cos^2\ \theta\ R_F(\theta, n)\ \mathrm{d}\theta$ (32, 45) are related to the reflectance $R_F(\theta, n)$ of an incident light ray with angle of incidence θ and the refractive index ratio $n = \frac{n_{med}}{n_{env}}$ between the medium (n_{med}) and the environment (n_{env}), which is computed by the Frensel equations (32, 45) and is given in *SI Appendix*, Eq. **S5**. The above equation degenerates to $I_{in} = 0$ in Eq. **4** for the refractive-index-matched boundary since $R_\phi = 0$ and $R_J = 0$.

The diffuse reflectance R_d represents the amount of light power leaving the medium and entering the surrounding environment through the boundary. Diffusion reflectance is a key observable quantity in optical experiments since it can be directly measured by a photodetector placed at the boundary. It is given by (28, 32, 45, 49, 50)

$$R_d = I_{out} - I_{in} = \mathbf{J}\cdot\mathbf{n}, \quad [6]$$

for no light source on the boundary. For a light source on the boundary, the above equation should be modified by subtracting the intensity of the light source from I_{in}.

Our Analytical Solution of the Diffusion Theory for an LED Source. A point LED source with power P, positioned at the origin in the cylindrical coordinates $(\rho, z) = (0, 0)$, is on the boundary $z = 0$ of a semi-infinite medium ($z \geq 0$) (Fig. 2*A*). There is no light source inside the medium such that Eq. **1** becomes

$$\mu_a\phi - D\nabla^2\phi = 0. \quad [7]$$

When the environment and the scattering medium have the same refractive index n, the incident intensity I_{in} equals the applied intensity $P\delta(x, y)$ (P—power of the point LED source, δ—2D Dirac delta function) such that Eq. **4** becomes

$$I_{in} = \frac{1}{4}\phi - \frac{1}{2}\mathbf{J}\cdot\mathbf{n} = P\delta(x, y) \ \text{ at } z = 0. \quad [8]$$

The diffuse reflectance R_d is modified from Eq. **6** by replacing I_{in} with $I_{in} - P\delta(x, y)$ to account for the light source on the boundary as

$$R_d = I_{out} - [I_{in} - P\delta(x, y)] = \mathbf{J}\cdot\mathbf{n} + P\delta(x, y). \quad [9]$$

Eq. **7** and its boundary condition Eq. **8** must be solved numerically [e.g., using finite element analysis (FEA)] to determine the light intensity ϕ inside the medium. To derive the analytical solution, ϕ in Eq. **8** is approximated using a first-order Taylor series around $z = -2D$, resulting in $\phi|_{z=-2D} = \phi|_{z=0} - 2D\mathrm{d}\phi/\mathrm{d}z|_{z=0}$ which eliminates the $\mathbf{J}\cdot\mathbf{n}$ term (45, 49–51) and yields

$$\frac{1}{4}\phi = P\delta(x, y) \quad \text{at } z = -2D. \quad [10]$$

This is called the extrapolated boundary condition (EBC). Eq. **7** and its approximate EBC (Eq. **10**) have an analytical solution

$$\phi(\rho, z) = P\frac{2\left(1 + \sqrt{\frac{\mu_a}{D}}r_0\right)(z + 2D)}{\pi r_0^3}\exp\left(-\sqrt{\frac{\mu_a}{D}}r_0\right), \quad [11]$$

where $r_0 = \sqrt{\rho^2 + (z+2D)^2}$. Eq. **11** is the Green's function for any LED source on the boundary. The diffuse reflectance on the boundary $z = 0$ is then obtained from Eq. **9**:

$$R_d = P\frac{2D}{\pi r_0^5}\left[r_0^2\left(1+\sqrt{\frac{\mu_a}{D}}r_0\right) - 4D^2\left(3+3\sqrt{\frac{\mu_a}{D}}r_0+\frac{\mu_a}{D}r_0^2\right)\right]\exp\left(-\sqrt{\frac{\mu_a}{D}}r_0\right) + P\delta(x,y). \quad [12]$$

Comparison of Our Analytical Solution and MC Simulations. To verify our analytical solution for LED (Eqs. **11** and **12**) and assess its applicability, we compare it with MC simulations, FEA results using the exact boundary condition Eq. **8**, and the existing analytical solution *SI Appendix*, Eqs. **S3** and **S4**, widely used for collimated light sources. In MC simulations, a point Lambertian source is applied on the boundary of a semi-infinite medium, with the representative optical properties of tissues $\mu_a = 0.005\ \text{mm}^{-1}$ and $\mu_s' = 2\ \text{mm}^{-1}$ (47, 52, 53), yielding a scattering length $1/\mu_s' = 0.5$ mm of the medium.

The intensity ϕ distributions beneath the source shown in Fig. 2 *B* and *C* clearly suggest that our analytical solution agrees well with the Lambertian MC simulation, except within 2 mm (4 times the scattering length $1/\mu_s'$) to the source. Beyond the depth of 2 mm, the difference is smaller than ~6%. The analytical solution (based on the approximate EBC Eq. **10**) is also very close to the FEA (based on the exact boundary condition Eq. **8**), suggesting that the EBC is quite accurate. In contrast, the existing analytical solution shows very large errors at small depths (Fig. 2*B* and *SI Appendix*, Fig. S2*A*), including a nonphysical singularity near the depth of 0.5 mm, leading to very large error (e.g., >1,000%). At 2 mm depth, its difference with MC simulation is 36%, much larger than ~6% for our analytical solution. For larger depths, such as 5 mm (Fig. 2*C* and *SI Appendix*, Fig. S2*A*), the errors are 28% and 0.7% for the existing and our analytical solutions, respectively. These observations also hold for other locations in the medium; *SI Appendix*, Fig. S1*C* shows the intensity along the z-axis for ρ =10 mm; at the same depth of 2 mm our analytical solution is accurate as compared to MC simulation (0.2% error), while the error in the existing analytical solution is 19%.

Fig. 2*D* shows the diffuse reflectance R_d; for radius ρ beyond 5 mm (10 times the scattering length of the medium), the difference between our analytical solution and Lambertian MC simulation is smaller than 3%, while the error based on the existing analytical solution is 23% (*SI Appendix*, Fig. S2*B*). This suggests that the photodetectors in experiments should be placed at least 10 times the scattering length of the medium from the light source when they are combined with our analytical solution to determine the optical properties of the medium.

Refractive-Index-Mismatched Boundary. The analysis above is limited to the refractive-index-matched boundary, where the medium and surrounding environment have the same refractive index, eliminating boundary reflections. For the general case of different refractive indices [e.g., biological tissues in air (46–48)], partial reflection occurs at the boundary. Consequently, both the boundary conditions Eq. **5** and the diffuse reflectance R_d in Eq. **6** must be modified.

For the refractive-index-mismatched boundary with an LED source, I_{in} is the sum of intensity from the LED source and the portion of I_{out} that is reflected back into the medium; Eq. **5** is then modified as

$$\frac{1}{4}\phi - \frac{1}{2}\mathbf{J}\cdot\mathbf{n} = \frac{R_\phi}{4}\phi + \frac{R_J}{2}\mathbf{J}\cdot\mathbf{n} + P'\delta(x,y) \quad \text{at } z = 0, \quad [13]$$

where $P' = (1 - R_{src})P$ represents the fraction of incident power that enters the scattering medium. Here, the source reflectance R_{src} is the fraction of incident power that reflects back to the environment and never enters the medium; it depends only on the refractive indices of environment and medium and can be analytically obtained from the Frensel equations (32, 45) (See *SI Appendix*, Note 2 for details). The diffuse reflectance R_d, modified from Eq. **6** to account for the LED source on the boundary, becomes

$$R_d = I_{out} - [I_{in} - P'\delta(x,y)] = \mathbf{J}\cdot\mathbf{n} + (1 - R_{src})P\delta(x,y), \quad [14]$$

which is identical to Eq. **9** except P is replaced by P'.

Eq. **7** and the boundary condition Eq. **13** can be solved by FEA. In order to obtain an approximate analytical solution, Eq. **13** is replaced by its corresponding EBC (45, 49, 50)

$$\frac{1}{4}\phi = \frac{1 - R_{src}}{1 - R_\phi}P\delta(x,y) \quad \text{at } z = -2C_R D, \quad [15]$$

where $C_R = (1 + R_J)/(1 - R_\phi)$. Eqs. **7** and **15** have the analytical solution, which is the Green's function for a boundary LED source:

$$\phi(\rho,z) = P\frac{2(1-R_{src})\left(1+\sqrt{\frac{\mu_a}{D}}r_0\right)(z+2C_R D)}{(1-R_\phi)\pi r_0^3}\exp\left(-\sqrt{\frac{\mu_a}{D}}r_0\right), \quad [16]$$

where $r_0 = \sqrt{\rho^2 + (z+2C_R D)^2}$. The diffuse reflectance at $z = 0$ is obtained from Eq. **14** as

$$R_d = P\frac{2D(1-R_{src})}{(1-R_\phi)\pi r_0^5}\left[r_0^2\left(1+\sqrt{\frac{\mu_a}{D}}r_0\right) - 4C_R^2D^2\left(3+3\sqrt{\frac{\mu_a}{D}}r_0+\frac{\mu_a}{D}r_0^2\right)\right]\exp\left(-\sqrt{\frac{\mu_a}{D}}r_0\right) + P'\delta(x,y), \quad [17]$$

An LED Embedded in an Infinite Medium. A point LED source with power P, positioned at the origin $(\rho, z) = (0, 0)$, is in an infinite medium to model a tissue with size much larger than the LED. The LED exhibits directional emission characteristics consistent with a Lambertian source (26, 33–35). As illustrated in Fig. 3*A*, its power irradiates exclusively within the positive z-hemisphere (maximum intensity along the $+z$ axis), with zero power applied in the negative z-hemisphere. The unit normal vector $\mathbf{n}$, pointing upward ($-z$ direction in Fig. 3*A*), is defined for the interface between the top ($z < 0$) and bottom ($z > 0$) halves of the medium. At the interface, the intensity into the bottom half is the sum of the intensity out of the top half and the power of the LED source:

$$I_{in,bottom} = I_{out,top} + P\delta(x,y), \quad [18]$$

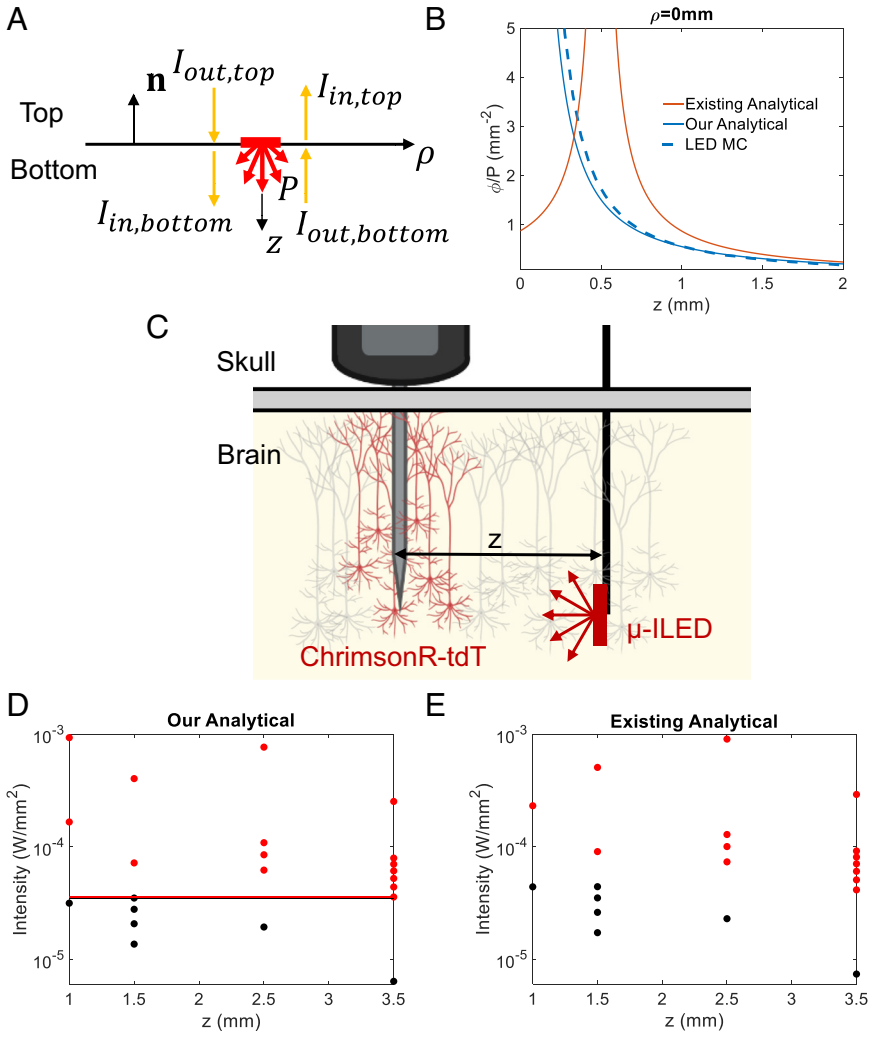

Fig. 3. Analytical solution of an LED in an infinite medium. (*A*) Schematic of an LED in an infinite medium. The LED irradiates exclusively into the *Bottom* half of the medium with the maximum intensity along the +*z* axis. The unit normal direction **n**, separating the *Top* and *Bottom* halves of the medium, points into the *Top* half. (*B*) Comparison of normalized intensity ϕ/P computed using MC simulations and analytical solutions along the *z* -axis near the LED. (*C*) Schematic of measurement setup for optogenetically evoked LFPs. (*D* and *E*) Irradiance threshold. Black and red dots represent nonactivated and activated cells in the experiments, respectively, based on (*D*) our analytical solution; (*E*) the existing analytical solution. (*D*) shows that a clear separation of black and red dots, which gives the irradiance threshold between 3.50×10^{-5} W/mm^2 (black horizontal line based on the highest black dot) and 3.58×10^{-5} W/mm^2 (red horizontal line based on the lowest red dot). The black and red dots in (*E*) cannot be separated by any horizontal line to give the irradiance threshold.

where $I_{out,top}$ represents the intensity of photons scattered within the top medium and propagating downward across the interface toward the bottom medium.

The intensity into the top half equals to the intensity out of the bottom half:

$$I_{out,bottom} = I_{in,top}, \quad [19]$$

where $I_{out,bottom}$ represents the intensity of photons scattered within the bottom medium and propagating upward across the interface toward the top medium.

They can be expressed in terms of the intensity ϕ as

$$\left(\frac{1}{4}\phi - \frac{1}{2}\mathbf{J}\cdot\mathbf{n}\right)|_{z=0^+} = \left(\frac{1}{4}\phi - \frac{1}{2}\mathbf{J}\cdot\mathbf{n}\right)|_{z=0^-} + P\delta(x,y), \quad [20]$$

$$\left(\frac{1}{4}\phi + \frac{1}{2}\mathbf{J}\cdot\mathbf{n}\right)|_{z=0^+} = \left(\frac{1}{4}\phi + \frac{1}{2}\mathbf{J}\cdot\mathbf{n}\right)|_{z=0^-}, \quad [21]$$

or equivalently

$$\frac{1}{4}\phi|_{z=0^+} = \frac{1}{4}\phi|_{z=0^-} + \frac{1}{2}P\delta(x,y), \quad [22]$$

$$\frac{1}{2}\mathbf{J}\cdot\mathbf{n}|_{z=0^+} = \frac{1}{2}\mathbf{J}\cdot\mathbf{n}|_{z=0^-} - \frac{1}{2}P\delta(x,y). \quad [23]$$

The analytical solution to Eq. **7** and the above continuity conditions Eqs. **22** and **23** is

$$\phi(\rho,z) = \frac{P}{4\pi r^3}\left[\frac{r^2}{D} + 2\left(1+\sqrt{\frac{\mu_a}{D}}r\right)z\right]\exp\left(-\sqrt{\frac{\mu_a}{D}}r\right), \quad [24]$$

where $r = \sqrt{\rho^2+z^2}$.

We compare the analytical solution Eq. **24** for an LED embedded in an infinite medium with MC simulations and the existing analytical solution in *SI Appendix*, Eq. **S11**. The intensity ϕ distributions beneath the source ($\rho = 0$) shown in Fig. 3*B* for $0 < z < 2$ mm demonstrate that our analytical solution agrees well with the Lambertian MC simulation and correctly predicts the singularity at the source, while the existing analytical solution exhibits a nonphysical singularity offset from the origin. Beyond 0.72 mm, the maximum errors are 120% and 6% for the existing and our analytical solutions, respectively.

Application #1: Determination of the Irradiance Threshold for Photostimulation. We first apply the our analytical solution Eq. **24** for an infinite medium to determine the irradiance threshold for photostimulation in the mouse brain. In this context, photostimulation refers to the optogenetic activation of cortical pyramidal neurons expressing the red-shifted opsin ChrimsonR (42) via illumination from a microscale inorganic LED (μ-ILED). Characterizing the irradiance threshold is crucial to ensure sufficient optical output in order to recruit neural responses effectively (54–56), while avoiding off-target effects such as local tissue heating from excessive photothermal effects (57). Once the irradiance threshold is determined, the analytical solution can be further used to estimate the minimal μ-ILED optical power required to activate neuronal populations at various distances, without the need for iterative MC simulations.

In our experiments (see details in *Materials and Methods*), we use a 0.3 mm × 0.3 mm × 0.1 mm μ-ILED that emits at 628 nm. We vary its optical power P controlled from 0.068 to 14 mW. The reported optical properties for brain at 628 nm are $\mu_a = 0.064\ \text{mm}^{-1}$ and $\mu_s' = 2.9\ \text{mm}^{-1}$ (58).

We record local field potentials (LFPs) from ChrimsonR-activated neurons in the primary somatosensory cortex using a multielectrode array. A filamentary probe supporting the μ-ILED is sequentially implanted at varying axial distances z = 1, 1.5, 2.5, and 3.5 mm (and ρ = 0 mm) from the recording electrodes (Fig. 3*C*). At each implantation distance, the LED is activated at multiple output power levels, and the evoked LFPs are recorded (*SI Appendix*, Fig. S6). We consider a response as an activation (red dots in Fig. 3*D*) if the recorded voltage change exceeds six SD above the baseline noise (59); smaller voltage changes are classified as nonactivations (black dots in Fig. 4*D*). The irradiance threshold corresponds to the light intensity value that separates the activation and nonactivation data points.

The mouse brain diameter [~10mm (60)] is significantly larger than both the LED dimensions and the 0.72 mm minimum distance required for diffusion theory validity (<6% error, Fig. 3*B*), thereby satisfying the infinite-medium approximation while ensuring the accuracy of our analytical solution Eq. **24**. The light intensity ϕ at each electrode is calculated using our analytical solution Eq. **24**, based on the LED optical power P and distance z (Fig. 3*C*) measured in the experiment. Black and red dots represent nonactivated and activated cells in the experiments, respectively (Fig. 3*D*). The data show that all nonactivation cases correspond to intensities below 3.50×10^{-5} W/mm^2 (the black line in Fig. 3*D*), whereas all activation cases occur above 3.58×10^{-5} W/mm^2 (the red line in Fig. 3*D*). Based on these results, we estimate an irradiance threshold of $(3.54 \pm 0.04) \times 10^{-5}$ W/mm^2, which lies within the range reported for ChrimsonR activation [3×10^{-6} to 5×10^{-4} W/mm^2 (42, 61)]. In contrast, the existing analytical solution in *SI Appendix*, Eq. **S11** fails to provide a threshold (Fig. 3*E*) as there can be no horizontal line to separate the black and red dots (the highest black dot is above the lowest red dot).

Application #2: Derivation of Tissue Properties from LED-Based Diffusion Reflectance. Derivation of tissue properties through fitting analytical solutions to the diffuse reflectance R_d acquired from photodetectors on the boundary of the sample is a widely employed approach, with critical applications in brain oxygen monitoring, cerebral hemodynamic assessment, and photobiomodulation (36–40). We demonstrate how our analytical solution designed for LED sources enables accurate derivation of tissue oxygen saturation (StO_2) and hemoglobin concentration (c).

Due to the distinct absorption spectra of oxyhemoglobin (HbO_2) and deoxyhemoglobin (Hb), StO_2 can be determined by fitting absorption coefficients at two wavelengths (62–64), typically one in the red and one in the near-infrared region. Here, we use 660 nm and 940 nm, which are commonly employed in clinical settings (65, 66). The absorption coefficients at these wavelengths, denoted as $\mu_{a,660}$ and $\mu_{a,940}$, arise from the contributions of HbO_2 and Hb, and their relationship can be expressed as (47, 67)

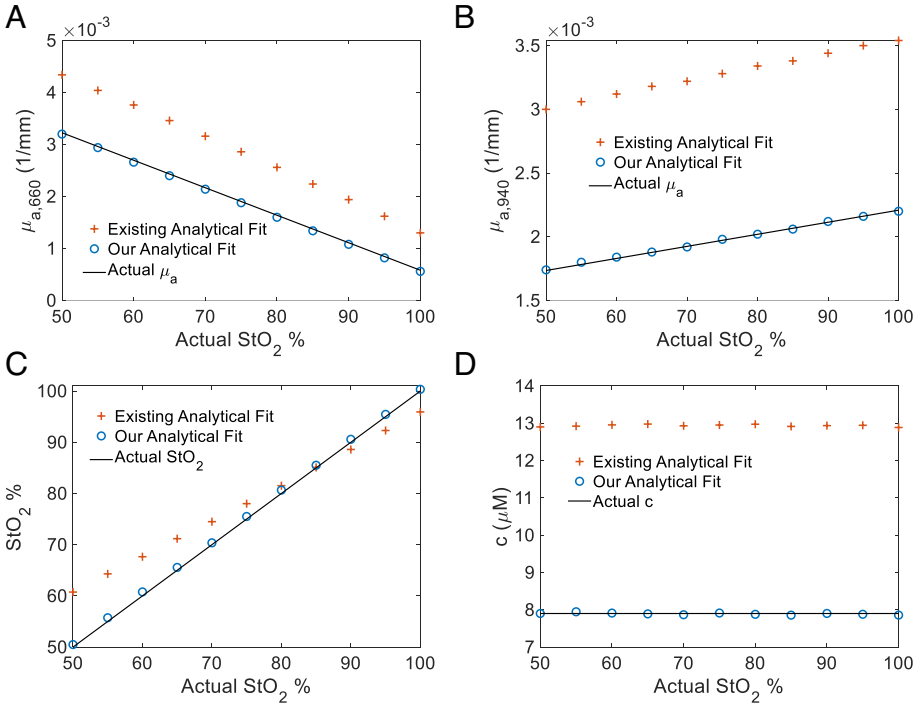

Fig. 4. Tissue property derivation based on our and existing analytical solutions and MC simulations. (*A*) $\mu_{a,660}$, (*B*) $\mu_{a,940}$, (*C*) StO_2, (*D*) the total hemoglobin concentration c derivation across a range of true StO_2 values. Fitting is performed at four detection distances (8, 10, 12, 14 mm) from the source. Black lines in all figures represent the actual properties in MC simulations.

$$\begin{bmatrix} \mu_{a,660} \\ \mu_{a,940} \end{bmatrix} = \ln 10 \begin{bmatrix} \varepsilon_{Hb,660} & \varepsilon_{HbO_2,660} \\ \varepsilon_{Hb,940} & \varepsilon_{HbO_2,940} \end{bmatrix} \begin{bmatrix} c_{Hb} \\ c_{HbO_2} \end{bmatrix}, \quad [25]$$

where $\varepsilon_{Hb,660} = 322.656\ \text{mm}^{-1}\ \text{M}^{-1}$ and $\varepsilon_{Hb,940} = 69.344\ \text{mm}^{-1}\ \text{M}^{-1}$ denote the molar extinction coefficient of Hb at 660 nm and 940 nm, respectively; and $\varepsilon_{HbO_2,660} = 31.96\ \text{mm}^{-1}\ \text{M}^{-1}$ and $\varepsilon_{HbO_2,940} = 121.4\ \text{mm}^{-1}\,\text{M}^{-1}$ denote the molar extinction coefficient of HbO_2 at 660 nm and 940 nm (67); c_{Hb} and c_{HbO_2} are concentrations of Hb and HbO_2, and $c = c_{Hb} + c_{HbO_2} = 7.9\ \mu\text{M}$ (47) is the total concentration of hemoglobin. For a given StO_2, $C_{HbO_2} = cStO_2$ and $C_{Hb} = c(1 - StO_2)$. The μ_s' of skin at 660 nm and 940 nm are 2.98 mm^{-1} and 1.99 mm^{-1}, respectively (47).

With known values of StO_2 and c, μ_a can be determined from Eq. **25**. Using MC simulations with known values of μ_a and μ_s', we generate synthetic R_d data points, then fit our analytical solution Eq. **12** in order to determine μ_a, and subsequently derive StO_2 and c. This allows us to quantitatively evaluate the accuracy of our method in deriving tissue properties.

The reflectance profiles to be fitted are generated using MC simulations of a point Lambertian source irradiating a semi-infinite medium. We systematically vary StO_2 from 50% to 100% while fixing c at 7.9 μM. To mitigate errors inherent in diffusion theory at very short distances (*SI Appendix*, Figs. S1*D* and S2*B*), we only include reflectance data for distance to the light source $\rho > 5$ mm. Additionally, MC data at very large distances are weak and random noise appears when $\rho > 18$ mm (*SI Appendix*, Fig. S3). Therefore, we extract 4 reflectance (R_d) points at ρ = 8, 10, 12, and 14 mm, simulating 4 photodetectors in experiments.

Fig. 4 *A* and *B* show the fitted $\mu_{a,660}$ and $\mu_{a,940}$ versus the actual μ_a used in MC simulations. During the fitting process, the reduced scattering coefficients at the respective wavelengths are treated as known parameters (62–64). All fitted μ_a are within 3.5% from the actual μ_a in Fig. 4 *A* and *B*. Therefore, our analytical solution is essential for accurately deriving μ_a from LED sources. In contrast, the existing analytical solution *SI Appendix*, Eq. **S4** for collimated sources leads to at least 35% error for μ_a in Fig. 4 *A* and *B*.

Once $\mu_{a,660}$ and $\mu_{a,940}$ are obtained by fitting, c_{Hb} and c_{HbO_2} can be calculated analytically by solving Eq. **25**. Then, $StO_2 = \frac{c_{HbO_2}}{c_{Hb} + c_{HbO_2}}$ and $c = c_{Hb} + c_{HbO_2}$. As shown in Fig. 4*C*, the computed StO_2 values deviate by less than 1.3% from the ground truth used in the MC simulations. Similarly, the error in the computed c values is below 0.6% (Fig. 4*D*). In contrast, the existing analytical solution for collimated sources (*SI Appendix*, Eq. **S4**) yields significantly higher errors: 22% for StO_2 and 64% for c.

Conclusion. We propose a method that accurately models light propagation in the scattering media with an LED source. The analytical solutions, derived for surface-mounted and embedded LEDs, demonstrate excellent agreement with MC simulations, while overcoming the systematic errors inherent in conventional collimated-source models. These analytical solutions have been successfully applied to solve the irradiance threshold for photostimulation in optogenetic experiments coupled with in vivo electrophysiology recordings and to derive optical properties (μ_a and μ_s') precisely from LED-based diffusion reflectance. These advances establish a rigorous theoretical foundation for optical measurements using LED sources, enabling the design of next-generation wearable and implantable biosensors with improved accuracy.

Materials and Methods

FEA of the Diffusion Equation. FEA is performed using COMSOL Multiphysics 6.0. The Helmholtz equation in the Mathematics module is employed to simulate light propagation in highly scattering media. The simulation domain is modeled as a block with dimensions large enough to minimize boundary effects. Mesh convergence is ensured to achieve accurate results. A source is applied at the center of the block surface as a small square region. Further reduction in the source size has a negligible impact on the region of interest. For the semi-infinite results shown in Fig. 2 *B* and *D*, the total computation time is 52 s with 53760 elements in a domain of 80 mm × 80 mm × 30 mm. The simulations are performed on a laptop equipped with a 12th Gen Intel® Core™ i9-12900H CPU and an NVIDIA GeForce RTX 3060 Laptop GPU.

MC Simulation. MC simulations were conducted using MCXLAB (13, 68). All media are modeled as blocks, with dimensions verified to be sufficiently large to avoid boundary effects on the studied region. The block is voxelated with a side length of 0.2 mm. A total of 5×10^9 photons are simulated in each run. A point source with a Lambertian profile is placed at the center of the top surface. For the semi-infinite results shown in Fig. 2 *B* and *D*, the total computation time is 23.7 min. Despite the high photon count, noticeable noise remains in regions beyond 18 mm from the source (*SI Appendix*, Fig. S3). The simulations are performed on a laptop equipped with a 12th Gen Intel® Core™ i9-12900H CPU and an NVIDIA GeForce RTX 3060 Laptop GPU. In contrast, our analytical solution is extremely efficient and capable of computing intensity or reflectance at 10,000 spatial points in MATLAB within just 3 milliseconds.

Measurement of Optogenetically Evoked LFPs. All procedures are approved by the Northwestern University Animal Care and Use Committee. C57BL/6 mice (Charles River, Wilmington, MA) are bred in-house and used. Mice are anesthetized with isoflurane (3% induction; 1.5 to 2% maintenance) and secured in a stereotaxic frame (David Kopf Instruments, Tujunga, CA). Analgesics included bupivacaine, meloxicam, and extended-release buprenorphine. AAV1.Syn-ChrimsonR-tdT (1×10^{13} GC/mL; Addgene #59171-AAV1, courtesy of Dr. Edward Boyden) (42) is injected into the primary somatosensory cortex (AP: 0.0 mm; ML: ±2.0 mm; DV: –0.5 mm) using a pulled glass micropipette (tip diameter: 7 to 10 μm) at 100 to 150 nL/min (total 200 nL) with an UltraMicroPump (World Precision Instruments, Sarasota, FL). Viral expression is allowed for 4 wk before recordings.

For electrophysiological recordings, the mice are anesthetized with isofluorane (3% induction; 1.5 to 2% maintenance) and secured in a stereotaxic frame. A 1.0 mm craniotomy is performed over the injected region. A stainless-steel screw (McMaster-Carr #90910A600) connected to a silver wire (Warner Instruments #64-1320) is implanted in the contralateral occiput as a reference. A custom headplate is affixed to the skull to stabilize the animal during recordings. A 64-channel, 4-shank multielectrode array (NeuroNexus, Ann Arbor, MI) is inserted so the tips of the probes are 1000 μm below the cortical surface and connected to an Intan C3325 amplifier. A separate filamentary probe carrying a single μ-ILED is introduced through lateral craniotomies at variable distances from the array using an independent stereotaxic arm. Optical pulses (2 ms) of varying output power are delivered via a Keithley 6221 precision current source (Tektronix, Beaverton, OR). Neural signals and μ-ILED currents are acquired at 30 kHz using an OpenEphys acquisition board (GUI version 0.5.5).

Offline analysis is conducted in Python. LFPs from all 200 trials per condition are averaged over a 25 ms poststimulation window. A response is classified as effective if the minimum LFP deflection exceeds 6 times the SD from the baseline (59).

Data, Materials, and Software Availability. All study data are included in the article and/or *SI Appendix*. Additional supporting data are available from Zenodo (https://doi.org/10.5281/zenodo.16615847) (69).

ACKNOWLEDGMENTS. This work was funded by the Querrey-Simpson Institute for Bioelectronics (M.W. ans J.A.R.); NINDS/BRAIN Initiative 1U01NS131406 (Y.K., M.W., and K.L.B.). Some schematics are created with BioRender.com.

Author affiliations: [a]Department of Civil and Environmental Engineering, Northwestern University, Evanston, IL 60208; [b]State Key Laboratory of Structural Analysis, Optimization and CAE Software for Industrial Equipment, Department of Engineering Mechanics, Dalian University of Technology, Dalian, Liaoning 116024, China; [c]Querrey Simpson Institute for Bioelectronics, Northwestern University, Evanston, IL 60208; [d]Department of Neurobiology, Northwestern University, Evanston, IL 60208; [e]Department of Mechanical Engineering, Northwestern University, Evanston, IL 60208; [f]Department of Biomedical Engineering, Northwestern University, Evanston, IL 60208; [g]Department of Materials Science and Engineering, Northwestern University, Evanston, IL 60208; and [h]Department of Neurological Surgery, Feinberg School of Medicine, Northwestern University, Chicago, IL 60611

1. F. F. Jöbsis, Noninvasive, infrared monitoring of cerebral and myocardial oxygen sufficiency and circulatory parameters. *Science* **198**, 1264–1267 (1977).
2. A. I. Efimov *et al.*, Remote optogenetic control of the enteric nervous system and brain-gut axis in freely-behaving mice enabled by a wireless, battery-free optoelectronic device. *Biosens. Bioelectron.* **258**, 116298 (2024).
3. R. Richards-Kortum, E. Sevick-Muraca, Quantitative optical spectroscopy for tissue diagnosis. *Ann. Rev. Phys. Chem.* **47**, 555–606 (1996).
4. R. Datta, T. M. Heaster, J. T. Sharick, A. A. Gillette, M. C. Skala, Fluorescence lifetime imaging microscopy: Fundamentals and advances in instrumentation, analysis, and applications. *J. Biomed. Opt.* **25**, 071203–071203 (2020).
5. F. Scholkmann *et al.*, A review on continuous wave functional near-infrared spectroscopy and imaging instrumentation and methodology. *Neuroimage* **85**, 6–27 (2014).
6. D. He, D. Malu, Y. Hu, A comprehensive review of indentation of gels and soft biological materials. *Appl. Mech. Rev.* **76**, 050802 (2024).
7. C. Park *et al.*, Adaptive electronics for photovoltaic, photoluminescent and photometric methods in power harvesting for wireless wearable sensors. *Nature Commun.* **16**, 5808 (2025).
8. Y. Zhang *et al.*, Millimetre-scale bioresorbable optoelectronic systems for electrotherapy. *Nature* **640**, 77–86 (2025).
9. M. Kim *et al.*, Wireless, battery-free, remote photoactivation of caged-morphine for photopharmacological pain modulation without side effects. *Biosens. Bioelectron.* **281**, 117440 (2025).
10. A. I. Efimov *et al.*, Remote optogenetic control of the enteric nervous system and brain-gut axis in freely-behaving mice enabled by a wireless, battery-free optoelectronic device. *Biosens. Bioelectron.* **258**, 116298 (2024).
11. J. H. Lee *et al.*, Deeply implantable, shape-morphing, 3D MicroLEDs for pancreatic cancer therapy. *Adv. Mater.* e2411494 (2024).
12. L. Wang, S. L. Jacques, L. Zheng, MCML–Monte Carlo modeling of light transport in multi-layered tissues. *Computer Methods Programs Biomed.* **47**, 131–146 (1995).
13. Q. Fang, D. A. Boas, Monte Carlo simulation of photon migration in 3D turbid media accelerated by graphics processing units. *Opt. Express* **17**, 20178–20190 (2009).
14. G. W. Lucassen, W. Verkruysse, M. Keijzer, M. J. van Gemert, Light distributions in a port wine stain model containing multiple cylindrical and curved blood vessels. *Lasers Surg. Med.* **18**, 345–357 (1996).
15. C. Zhu, Q. Liu, Validity of the semi-infinite tumor model in diffuse reflectance spectroscopy for epithelial cancer diagnosis: A Monte Carlo study. *Opt. Express* **19**, 17799–17812 (2011).
16. A. Ishimaru, Diffusion of light in turbid material. *Appl. Opt.* **28**, 2210–2215 (1989).
17. M. S. Patterson, B. Chance, B. C. Wilson, Time resolved reflectance and transmittance for the noninvasive measurement of tissue optical properties. *Appl. Opt.* **28**, 2331–2336 (1989).
18. T. J. Farrell, M. S. Patterson, B. Wilson, A diffusion theory model of spatially resolved, steady-state diffuse reflectance for the noninvasive determination of tissue optical properties in vivo. *Med. Phys.* **19**, 879–888 (1992).
19. W. Lu *et al.*, Wireless, implantable catheter-type oximeter designed for cardiac oxygen saturation. *Sci. Adv.* **7**, eabe0579 (2021).
20. J. G. Webster, *Design of Pulse Oximeters* (CRC Press, 1997).
21. W. Ouyang *et al.*, A wireless and battery-less implant for multimodal closed-loop neuromodulation in small animals. *Nature Biomed. Eng.* **7**, 1252–1269 (2023).
22. D. Franklin *et al.*, Synchronized wearables for the detection of haemodynamic states via electrocardiography and multispectral photoplethysmography. *Nature Biomed. Eng.* **7**, 1229–1241 (2023).
23. M. A. Q. Siddiqui, K. Regenauer-Lieb, H. Roshan, Thermo-hydro-chemo-mechanical (THCM) continuum modeling of subsurface rocks: A focus on thermodynamics-based constitutive models. *Appl. Mech. Rev.* **76**, 031001 (2024).
24. B. C. Wilson, G. Adam, A Monte Carlo model for the absorption and flux distributions of light in tissue. *Med. Phys.* **10**, 824–830 (1983).
25. C. Zhu, Q. Liu, Review of Monte Carlo modeling of light transport in tissues. *J. Biomed. Opt.* **18**, 050902 (2013).
26. M. Schweiger, S. R. Arridge, M. Hiraoka, D. T. Delpy, The finite element method for the propagation of light in scattering media: Boundary and source conditions. *Med. Phys.* **22**, 1779–1792 (1995).
27. V. V. Tuchin, Tissue optics and photonics: Light-tissue interaction. *J. Biomed. Photon. Eng.* **1**, 3–54 (2015).
28. M. Keijzer, W. M. Star, P. R. Storchi, Optical diffusion in layered media. *Appl. Opt.* **27**, 1820–1824 (1988).
29. G. Eason, A. Veitch, R. Nisbet, F. Turnbull, The theory of the back-scattering of light by blood. *J. Phys. D: Appl. Phys.* **11**, 1463 (1978).
30. R. J. Fretterd, R. L. Longini, Diffusion dipole source. *J. Opt. Soc. Am.* **63**, 336–337 (1973).
31. R. Hirko, R. Fretterd, R. Longini, Application of the diffusion dipole to modelling the optical characteristics of blood. *Med. Biol. Eng.* **13**, 192–195 (1975).
32. L. V. Wang, H.-I. Wu, *Biomedical Optics: Principles and Imaging* (John Wiley & Sons, 2007).
33. E. Khaidarov *et al.*, Control of LED emission with functional dielectric metasurfaces. *Laser Photon. Rev.* **14**, 1900235 (2020).
34. Y. Huang, E.-L. Hsiang, M.-Y. Deng, S.-T. Wu, Micro-LED, Micro-LED and OLED displays: Present status and future perspectives. *Light: Sci. Appl.* **9**, 105 (2020).
35. N. C. Greenham, R. H. Friend, D. D. Bradley, Angular dependence of the emission from a conjugated polymer light-emitting diode: Implications for efficiency calculations. *Adv. Mater.* **6**, 491–494 (1994).
36. K.-S. Hong, M. J. Khan, M. J. Hong, Feature extraction and classification methods for hybrid fNIRS-EEG brain-computer interfaces. *Front. Human Neurosci.* **12**, 246 (2018).
37. K. D. Desmet *et al.*, Clinical and experimental applications of NIR-LED photobiomodulation. *Photomed. Laser Ther.* **24**, 121–128 (2006).
38. W. T. Huang *et al.*, Near-infrared windows I and II phosphors for theranostic applications: Spectroscopy, bioimaging, and light-emitting diode photobiomodulation. *Adv. Opt. Mater.* **11**, 2202061 (2023).
39. A. J. Metz, S. Klein, F. Scholkmann, U. Wolf, Continuous coloured light altered human brain haemodynamics and oxygenation assessed by systemic physiology augmented functional near-infrared spectroscopy. *Sci. Rep.* **7**, 10027 (2017).
40. M. A. Yücel *et al.*, Best practices for fNIRS publications. *Neurophotonics* **8**, 012101 (2021).
41. X. Wang, X. Yang, J. Mei, K. Zhao, Mechanics and dynamics of organic mixed ionic–electronic conductors. *Appl. Mech. Rev.* **77**, 1–108 (2025).
42. N. C. Klapoetke *et al.*, Independent optical excitation of distinct neural populations. *Nature Methods* **11**, 338–346 (2014).
43. M. Dehghany, H. Zhang, R. Naghdabadi, Y. Hu, A thermodynamically-consistent large deformation theory coupling photochemical reaction and electrochemistry for light-responsive gels. *J. Mech. Phys. Solids* **116**, 239–266 (2018).
44. M. F. Modest, S. Mazumder, *Radiative Heat Transfer* (Academic press, 2021).
45. R. C. Haskell *et al.*, Boundary conditions for the diffusion equation in radiative transfer. *JOSA A* **11**, 2727–2741 (1994).
46. J. L. Reuss, Multilayer modeling of reflectance pulse oximetry. *IEEE Trans. Biomed. Eng.* **52**, 153–159 (2005).
47. S. L. Jacques, Optical properties of biological tissues: A review. *Phys. Med. Biol.* **58**, R37 (2013).
48. R. Khan, B. Gul, S. Khan, H. Nisar, I. Ahmad, Refractive index of biological tissues: Review, measurement techniques, and applications. *Photodiagnosis Photodyn. Ther.* **33**, 102192 (2021).
49. A. Kienle, M. S. Patterson, Improved solutions of the steady-state and the time-resolved diffusion equations for reflectance from a semi-infinite turbid medium. *JOSA A* **14**, 246–254 (1997).
50. A. H. Hielscher, S. L. Jacques, L. Wang, F. Tittel, The influence of boundary conditions on the accuracy of diffusion theory in time-resolved reflectance spectroscopy of biological tissues. *Phys. Med. Biol.* **40**, 1957 (1995).
51. W. L. Vos, T. W. Tukker, A. P. Mosk, A. Lagendijk, W. L. IJzerman, Broadband mean free path of diffuse light in polydisperse ensembles of scatterers for white light-emitting diode lighting. *Appl. Opt.* **52**, 2602–2609 (2013).
52. G. Alexandrakis, F. R. Rannou, A. F. Chatziioannou, Tomographic bioluminescence imaging by use of a combined optical-PET (OPET) system: A computer simulation feasibility study. *Phys. Med. Biol.* **50**, 4225 (2005).
53. J. L. Sandell, T. C. Zhu, A review of in-vivo optical properties of human tissues and its impact on PDT. *J. Biophoton.* **4**, 773–787 (2011).
54. V. Emiliani *et al.*, Optogenetics for light control of biological systems. *Nature Rev. Methods Primers* **2**, 55 (2022).
55. J. Y. Lin, A user's guide to channelrhodopsin variants: Features, limitations and future developments. *Exp. Physiology* **96**, 19–25 (2011).
56. J. C. Williams *et al.*, Computational optogenetics: Empirically-derived voltage-and light-sensitive channelrhodopsin-2 model. *PLoS Comput. Biol.* **9**, e1003220 (2013).
57. S. F. Owen, M. H. Liu, A. C. Kreitzer, Thermal constraints on in vivo optogenetic manipulations. *Nature Neurosci.* **22**, 1061–1065 (2019).
58. P. Van der Zee, M. Essenpreis, D. T. Delpy, "Optical properties of brain tissue" in *Photon Migration and Imaging in Random Media and Tissues (SPIE)* (1993), pp 454–465.
59. R. Q. Quiroga, Z. Nadasdy, Y. Ben-Shaul, Unsupervised spike detection and sorting with wavelets and superparamagnetic clustering. *Neural Comput.* **16**, 1661–1687 (2004).
60. A. Badea, A. A. Ali-Sharief, G. A. Johnson, Morphometric analysis of the C57BL/6J mouse brain. *Neuroimage* **37**, 683–693 (2007).
61. G. Gauvain *et al.*, Optogenetic therapy: High spatiotemporal resolution and pattern discrimination compatible with vision restoration in non-human primates. *Commun. Biol.* **4**, 125 (2021).
62. C. Wu *et al.*, A wireless near-infrared spectroscopy device for flap monitoring: Proof of concept in a porcine musculocutaneous flap model. *J. Reconstr. Microsurg.* **38**, 96–105 (2022).
63. A. Y. Rwei *et al.*, A wireless, skin-interfaced biosensor for cerebral hemodynamic monitoring in pediatric care. *Proc. Nat. Acad. Sci.* **117**, 31674–31684 (2020).
64. M. Lindkvist, G. Granåsen, C. Grönlund, Coherent derivation of equations for differential spectroscopy and spatially resolved spectroscopy: An undergraduate tutorial. *Spectroscopy Lett.* **46**, 243–249 (2013).
65. S. Chatterjee, J. P. Phillips, P. A. Kyriacou, Monte Carlo investigation of the effect of blood volume and oxygen saturation on optical path in reflectance pulse oximetry. *Biomed. Phys. Eng. Express* **2**, 065018 (2016).
66. P. Kyriacou, K. Budidha, T. Y. Abay, Optical techniques for blood and tissue oxygenation. *Encycl. Biomed. Eng.* **3**, 461–472 (2019).
67. S. Prahl, Optical abSorption of hemoglobin. https://omlc.org/spectra/hemoglobin/. Accessed 1 March 2025.
68. L. Yu, F. Nina-Paravecino, D. Kaeli, Q. Fang, Scalable and massively parallel Monte Carlo photon transport simulations for heterogeneous computing platforms. *J. Biomed. Opt.* **23**, 010504 (2018).
69. H. Zhang, M. Wu, K. Bodkin, Y. Huang, Data for the article "Analytical solutions for light propagation of LED." Zenodo. https://doi.org/10.5281/zenodo.16615847 Deposited 30 July 2025.